AGU PUBLICATIONS

JGR

Journal of Geophysical Research: Space Physics

RESEARCH ARTICLE

10.1002/2015JA021790

Key Points:

- The electrodynamic structure of a Sun-aligned arc is resolved in time and space
- Plasma density depletion formed by intense E fields and FACs of Sun-aligned arc
- Large E fields and ion temperatures are collocated with the density depletion

Supporting Information:

- Movie S1
- Movie S2
- Movies S1 and S2 Captions

Correspondence to:
G. W. Perry,
perry@phys.ucalgary.ca

Citation:
Perry, G. W., H. Dahlgren, M. J. Nicolls, M. Zettergren, J.-P. St.-Maurice, J. L. Semeter, T. Sundberg, K. Hosokawa, K. Shiokawa, and S. Chen (2015), Spatiotemporally resolved electrodynamic properties of a Sun-aligned arc over Resolute Bay, *J. Geophys. Res. Space Physics*, *120*, 9977–9987, doi:10.1002/2015JA021790.

Received 10 AUG 2015
Accepted 15 OCT 2015
Accepted article online 20 OCT 2015
Published online 17 NOV 2015

Spatiotemporally resolved electrodynamic properties of a Sun-aligned arc over Resolute Bay

G. W. Perry[1,2], H. Dahlgren[3,4], M. J. Nicolls[5], M. Zettergren[6], J.-P. St.-Maurice[1], J. L. Semeter[7], T. Sundberg[8], K. Hosokawa[9], K. Shiokawa[10], and S. Chen[5]

[1]Institute of Space and Atmospheric Studies, University of Saskatchewan, Saskatoon, Saskatchewan, Canada, [2]Now at Department of Physics and Astronomy, University of Calgary, Canada, [3]KTH Royal Institute of Technology, Stockholm, Sweden, [4]School of Physics and Astronomy, University of Southampton, Southampton, UK, [5]SRI International, Menlo Park, California, USA, [6]Physical Sciences Department, Embry-Riddle Aeronautical University, Daytona Beach, Florida, USA, [7]Department of Electrical and Computer Engineering and Center for Space Physics, Boston University, Boston, Massachusetts, USA, [8]School of Physics and Astronomy, Queen Mary University of London, London, UK, [9]Department of Communication Engineering and Informatics, University of Electro-Communications, Chofu, Japan, [10]Institute for Space-Earth Environmental Research, Nagoya University, Nagoya, Japan

Abstract Common volume measurements by the Resolute Bay Incoherent Scatter Radar-North (RISR-N) and Optical Mesosphere and Thermosphere Imagers (OMTI) have been used to clarify the electrodynamic structure of a Sun-aligned arc in the polar cap. The plasma parameters of the dusk-to-dawn drifting arc and surrounding ionosphere are extracted using the volumetric imaging capabilities of RISR-N. Multipoint line-of-sight RISR-N measurements of the plasma drift are inverted to construct a time sequence of the electric field and field-aligned current system of the arc. Evidence of dramatic electrodynamic and plasma structuring of the polar cap ionosphere due to the arc is described. One notable feature of the arc is a meridionally extended plasma density depletion on its leading edge, located partially within a downward field-aligned current region. The depletion is determined to be a by-product of enhanced chemical recombination operating on a time scale of 15 min. A similarly shaped electric field structure of over 100 mV/m and line-of-sight ion temperatures nearing 3000 K were collocated with the depletion.

1. Introduction

Sun-aligned arcs are the hallmark of a polar ionosphere under northward interplanetary magnetic field (IMF) conditions [*Carlson and Cowley*, 2005]. The arcs are often referred to as transpolar arcs, of which there are many identifiable types and classifications [*Kullen*, 2012]. *Zhu et al.* [1997] provide a review on the electrodynamic properties of Sun-aligned arcs. Many of the models, measurements, and conjectures regarding Sun-aligned arcs agree on a few features. First, the optical emissions of a Sun-aligned arc mark the location of an upward field-aligned current (FAC), carried by precipitating electrons. The magnetospheric source and energization mechanisms of the electrons remain unresolved; both soft and hard precipitation have been measured in the arcs. Corresponding downward FACs have been measured with the arcs [e.g., *Cumnock et al.*, 2011, and references therein], and sometimes multiple FAC pairs are detected. The arcs superpose an electric field on the background polar cap electric field, which can establish velocity shears in the polar cap convection [*Carlson et al.*, 1984; *Koustov et al.*, 2012].

Sun-aligned arcs are intrinsically linked to processes in the magnetosphere and its interaction with the solar wind [*Zhu et al.*, 1993a; *Hosokawa et al.*, 2011; *Fear and Milan*, 2012; *Fear et al.*, 2014]. Their interconnection to polar cap dynamics and structuring via magnetosphere-ionosphere (MI) coupling has been thoroughly investigated, although a complete understanding of its mediators and agents remains elusive. *Zhu et al.* [1993b] noted that inhomogeneities in the Pedersen conductivity are nontrivial in MI coupling. They alter the reflection coefficient of the ionosphere and can cause a rotation between the wave field of an incident and reflected Alfvén wave. For further insight into MI coupling in the polar cap, its impact on the plasma structuring and electrodynamics of the region must be investigated in detail. To accomplish this, accurate and spatiotemporally resolved diagnostics of the ionospheric component of the MI system are required.

The electrodynamics of Sun-aligned arcs is measured indirectly by estimating horizontal electric fields, from Doppler velocity measurements of plasma drifts obtained with radar [e.g., *Carlson et al.*, 1984]. Seminal work in this technique includes *de la Beaujardiere et al.* [1977] who used the Chatanika incoherent scatter radar (ISR) to estimate the current structure of three auroral arcs, with estimates of upward FACs measuring 6 and 9 μA/m^2 for two of them. ISRs also provide valuable diagnostic information of the electron density, n_e, and the ion and electron temperature, T_i and T_e, in the plasma. *Carlson et al.* [1984] measured a fourfold n_e increase within a Sun-aligned arc, consistent with plasma production by soft electron precipitation. They also detected significant T_i enhancements in the vicinity of velocity shears associated with the arc, a signature of frictional heating. Using the (European Incoherent Scatter Scientific Association) EISCAT radar, *Opgenoorth et al.* [1990] also identified enhanced T_i values located on the edges of auroral arcs. The location of the enhanced T_i was coincident with significant n_e depletions, both a result of strong electric fields (some approaching 125 mV/m) and enhanced chemical recombination rates.

Previous Sun-aligned arc research with ISR was conducted using a single, steerable antenna. With the development of the Advanced Modular Incoherent Scatter Radar (AMISR) systems and their electronic beam steering capabilities [*Nicolls and Heinselman*, 2007; *Bahcivan et al.*, 2010], it is now possible to investigate the electrodynamics of polar cap arcs, with multiple beams in a customized beam configuration which can encompass a large volume of the ionosphere. The beam is directed by adjusting the phase of the signals from the many antenna elements on a pulse-to-pulse basis, eliminating the need to mechanically steer a radar dish. In this way, volumetric measurements are provided without spatiotemporal ambiguities when integrating the measurements on the order of minutes [e.g., *Dahlgren et al.*, 2012a, 2012b]. With multiple beam configurations, one can also avoid many of the drawbacks inherent to estimating important parameters such as plasma drift from a single radar site, described in detail by *Freeman et al.* [1991]. For example, an assumption of spatially uniform mesoscale flow between measurements can be relaxed using simultaneous measurements from multiple beams. However, many of the limitations of a monostatic radar still apply; for example, the radar will always be insensitive to flow perpendicular to its line of sight and thus, without additional information, to mesoscale flow curvature [e.g., *Freeman et al.*, 1991].

In this paper we present a novel experimental perspective to polar cap dynamics and MI coupling by providing the first spatiotemporally resolved images of the organization and morphology of the ionospheric plasma and electric fields for a Sun-aligned arc. The data show a clear connection between the structuring in the *F* region polar cap ionosphere and the electrodynamics of the Sun-aligned arc. In particular, we provide direct estimates of auroral arc electric fields, current systems, and associated plasma density cavities. We demonstrate that these observations are consistent with existing arc models and dynamic plasma structuring mechanisms. Our observations confirm that intense electric fields and FACs are sufficient enough to ignite strong chemical recombination and current closure processes giving rise to the depletions. These processes have been demonstrated indirectly in the auroral zone [e.g., *Zettergren et al.*, 2014]; we report a direct confirmation that they are present in Sun-aligned arcs as well.

2. Observations and Instrumentation

For a more general overview of the Sun-aligned arc event described here, including information about the IMF conditions and a discussion on the possible generation mechanism of the arc, we direct the reader to *Dahlgren et al.* [2014].

2.1. Optical Mesosphere and Thermosphere Imagers

At 05:04 UT (approximately 22 magnetic local time (MLT)), on 20 February 2012, two closely separated Sun-aligned arcs became visible on the duskward edge of the field of view (FOV) of the Optical Mesosphere and Thermosphere Imagers (OMTI) all-sky imager installed at Resolute Bay, Canada (74.73°N, 265.07°E, geographic) [*Shiokawa et al.*, 1999]. A movie of both arcs moving through the Resolute Bay Incoherent Scatter Radar-North (RISR-N) FOV is provided as supporting information Movie S1. Both arcs traveled toward dawn (eastward) and were identifiable and collocated at the 557.7 and 630 nm wavelengths. At 05:14 UT, the arcs were near the zenith of the OMTI imager. The leading arc was much less intense than the trailing arc, at both optical wavelengths, and became indistinguishable from the brighter, trailing arc by 05:16 UT. It could not be determined whether the leading arc ceased to exist or was rendered indistinguishable due to a parallax effect. The brighter arc, hereafter referred to as the "arc," remained visible until 05:26 UT. During its transit, the luminosity of the arc varied between 350 and 450 R in the red line and green line emissions. The arc event studied here was one of many arcs passing through the region at this time. Several arcs were observed in the optical data, within minutes of the event studied here.

10.1002/2015JA021790

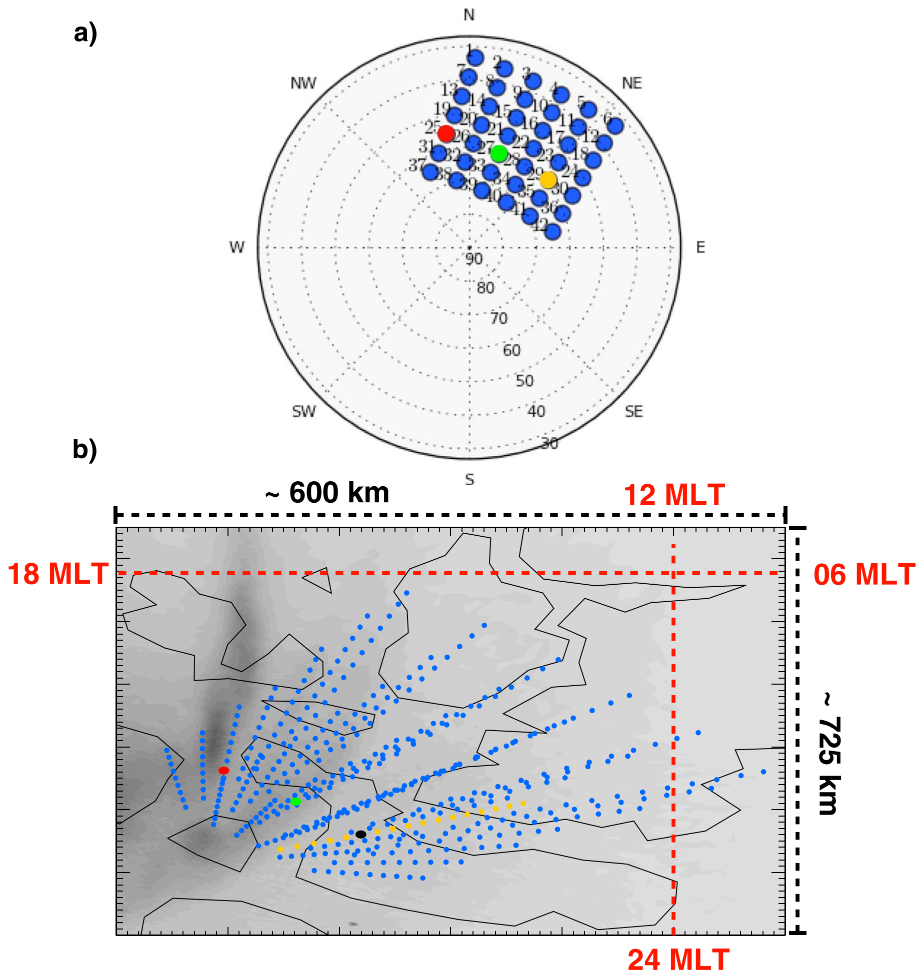

Figure 1. (a) The elevation angles and bearings of the 42 RISR-N beams used on 20 February 2012. The geographic directions are indicated. (b) The pierce points of the 42 RISR-N beams between 200 and 500 km altitude, plotted along with the OMTI data from 05:08 UT in gray scale. The orientation of the optical data has been flipped from its orientation in Movie S1 so that geographic north and east are on the top and right, respectively. The orange colored points indicate the pierce points from RISR-N beam 29 for all range gates along the beam. The red, green, and black points are the pierce points for beams 25, 27, and 29, respectively, at 285 km altitude. The dimensions of the RISR-N FOV and MLT meridians are indicated in black and red, respectively. The black contours are the geographic coastlines in the region.

2.2. RISR-N

At 05:06 UT, the arc entered the duskward edge of the RISR-N FOV, an AMISR class radar installed at Resolute Bay. RISR-N transmits at 441.9 MHz, providing diagnostic measurements of the polar ionosphere, including n_e, T_i, T_e, and line-of-sight (LOS) ion velocity measurements, v_{los}. For this study, the RISR-N was operating with a custom 42 beam mode, in a 6 × 7 grid, which is shown as a grid of black circles in Movie S1. The elevation angles and bearings of all the 42 RISR-N beams are plotted in Figure 1a as well as the geographic directions are labeled. In addition, the pierce points of all of the RISR-N beams located between 200 and 500 km altitude, the geographic coastlines of the region and the OMTI data showing the 630.0 nm emissions (in gray scale) at 05:08 UT are plotted in Figure 1b. The orange colored points show the pierce points of RISR-N beam 29 which will be discussed in more detail shortly. The system transmitted interleaved Barker and long-pulse coded radar pulses, giving approximately 750 m and 36 km range resolutions, respectively. The arc moved with an average speed of 250 m/s toward dawn and exited the RISR-N FOV at 05:22 UT.

A plot of n_e, $T_{i_{los}}$, T_e, and v_{los} as a function of time, measured in RISR-N beam 29 with the 2 min integrated long-pulse mode is given in Figure 2. All of the RISR-N data used in this work are 2 min integrated data. We have chosen to label the ion temperatures as $T_{i_{los}}$ for reasons that will be explained shortly. A time series of n_e measured at 285 km altitude in beams 25, 27, and 29, which are along a row in the RISR-N FOV

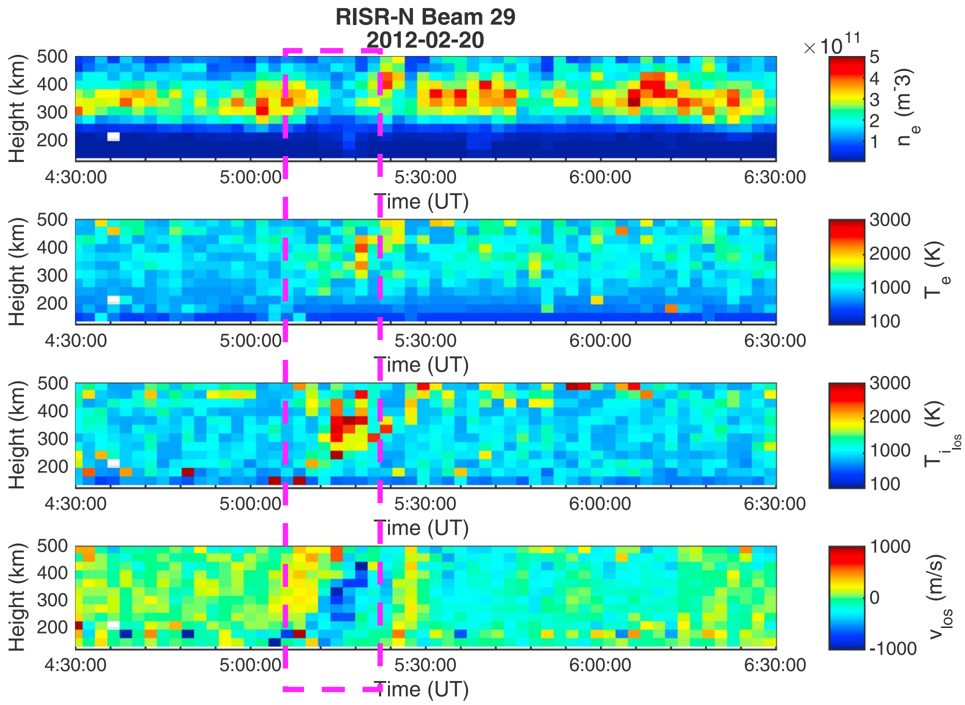

Figure 2. RISR-N beam 29 measurements of n_e, T_e, $T_{i_{los}}$, and v_{los}, as a function of altitude along the beam, and time. The time segment in which the Sun-aligned arc was within the RISR-N FOV is indicated by the violet, dashed box. This plot was produced with 2 min integrated data.

(colored red, green, and black, respectively, in Figure 1) is plotted in Figure 3. In Figures 2 and 3 the time segment during which the optical arc was seen to be within the RISR-N FOV is outlined by a violet, dashed box. The associated errors with the RISR-N measurements were very reasonable. The n_e errors are plotted in Figure 3 and are low. The v_{los} errors were also low; 70% of the measurements had a relative error below 25%.

A substantial n_e depletion region is seen in Figures 2 and 3 centered at approximately 05:12 UT in beam 29. The n_e decreased from 4.6 to almost 1.3×10^{11} m^{-3} in 10 min, starting at 05:02 UT. Measurements from adjacent beams show that the depletion progressed toward dawn, from beam 25 to 29. The depletion feature is marked by a shaded box colored for each beam in Figure 3. At 130 km altitude (not visible in any figure), an increase in n_e from 1 to 3×10^{10} m^{-3} was measured with the long-pulse mode. The enhancement was centered at 05:16 UT which is marked by a yellow shaded box in Figure 3. The increase was short-lived and was only present in beam 29 between 05:14 and 05:18 UT. A similar n_e enhancement was also measured with the Barker code mode (not presented here), although those observations are less reliable due to their relatively high measurement uncertainties. A more subtle signature of an n_e increase is indicated by the appearance of larger n_e values plotted below 200 km altitude in Figure 2, starting just after 05:12 UT. The n_e enhancement in the lower *F* region marks the arrival of the electron precipitation region of the optical arc in RISR-N beam 29, which trailed the n_e depletion feature on its dawnward trajectory. The appearance and ordering of the aforementioned signatures are evident in nearly all of the other beams in the RISR-N FOV.

During the arc event, both T_e and $T_{i_{los}}$ in beam 29 increased dramatically, each changing from 800 K to above 2500 K over several minutes, starting at 05:02 UT. The $T_{i_{los}}$ enhancement was collocated with the n_e depletion region as it moved through the RISR-N FOV and maximized at 3000 K for several minutes, starting at 05:16 UT. T_e reached 2500 K at approximately 05:20 UT, and only briefly maintained this temperature. In the majority of the RISR-N beams, the $T_{i_{los}}$ increases were measured into the lower *F* region, in some cases down to 175 km altitude. The T_e increases displayed a different characteristic and only generally stayed above 250 km altitude.

3. Analysis

In this paper we focus on the plasma and electrodynamic structuring of the arc observed over Resolute Bay. A technique that was developed by *Nicolls et al.* [2014] was used to estimate the electric fields within the RISR-N

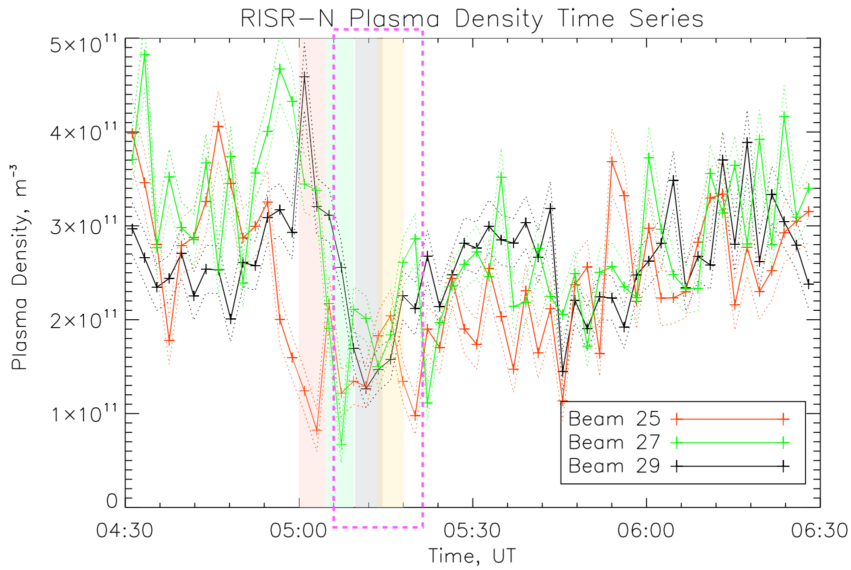

Figure 3. A time series of n_e measured at 285 km altitude in RISR-N beams 25 (red), 27 (green), and 29 (black), with associated error bars (dotted lines). These beams are also indicated in Figure 1. The time segment in which the arc was observed within the RISR-N FOV is outlined by a violet, dashed box. The shaded rectangles denote the approximate location of the plasma density depletion in each beam. The yellow shaded rectangle marks the appearance of the lower *F* region n_e enhancement.

FOV during the arc event. The approach centers on modeling a spatially varying electrostatic potential, ϕ, that reproduces the RISR-N v_{los} measurements. When a suitable ϕ is determined, the electric field, $\mathbf{E}_\perp$, is computed from $\mathbf{E} = -\nabla\phi$.

The *Nicolls et al.* [2014] method used here employs a superposition of two velocity fields over the RISR-N FOV. One field is a uniform "background" flow, $\mathbf{v}_0$, and superposed on it is a spatially varying velocity field, $\delta\mathbf{E}\times\mathbf{B}/|B|^2$, such that

$$\mathbf{v} = \mathbf{v}_\perp + \mathbf{v}_\parallel = \mathbf{v}_0 + \delta\mathbf{E}\times\mathbf{B}/|B|^2. \quad (1)$$

The background velocity field, $\mathbf{v}_0$, is determined using an inversion technique described by *Heinselman and Nicolls* [2008]. Variations on this background field, $\tilde{\mathbf{v}}_{\text{los}}$, are calculated by subtracting it from the measured RISR-N LOS measurements:

$$\tilde{\mathbf{v}}_{\text{los}} = \mathbf{v}_{\text{los}} - \mathbf{A}\mathbf{v}_0^\dagger, \quad (2)$$

in which $\mathbf{A}$ is an array representing the geometry of the RISR-N beams with respect to the geomagnetic field, and "$\dagger$" denotes a transpose operation. We assume that the plasma velocity is described sufficiently by the convection velocity flow (i.e., the plasma is incompressible) and that the convection electric field can be expressed as the gradient of an electrostatic potential, ϕ. Both are appropriate for the *F* region ionosphere in this case. Thus, the RISR-N LOS velocity measurements, $\mathbf{v}_{\text{los}}$, can be written as follows:

$$\mathbf{v}_{\text{los}} = \mathbf{A}\mathbf{v}_0^\dagger - \mathbf{T}\nabla^\dagger\phi + \mathbf{e}_{\text{los}}, \quad (3)$$

in which $\mathbf{T} = \mathbf{B}\times\mathbf{A}/|B|^2$, and $\mathbf{e}_{\text{los}}$ is the error. *Nicolls et al.* [2014] identified the problem of solving for a potential, ϕ, that accurately reproduces $\mathbf{v}_{\text{los}}$, from which $\mathbf{E}$ can be calculated, as one of constrained minimization. This is a highly underdetermined problem. Among the solutions that achieve the most probable tightness of fit to the data, the algorithm chooses the one that minimizes the mean squared curvature of the electric field within the measurement region and the absolute gradient outside of the measurement region. In doing so, features in ϕ must be well supported by the RISR-N measurements.

The *Nicolls et al.* [2014] technique builds and improves on previous work by *Heinselman and Nicolls* [2008] and *Butler et al.* [2010], who developed effective procedures for inverting RISR-N v_{los} measurements into full velocity vectors. However, those previous methods had difficulty reproducing vectors in the presence of velocity shears, such as those measured with this event, i.e., the shear appearing just after 05:00 UT in Figure 2. It is important to reiterate that we are not measuring plasma velocity vectors with this method or with RISR-N,

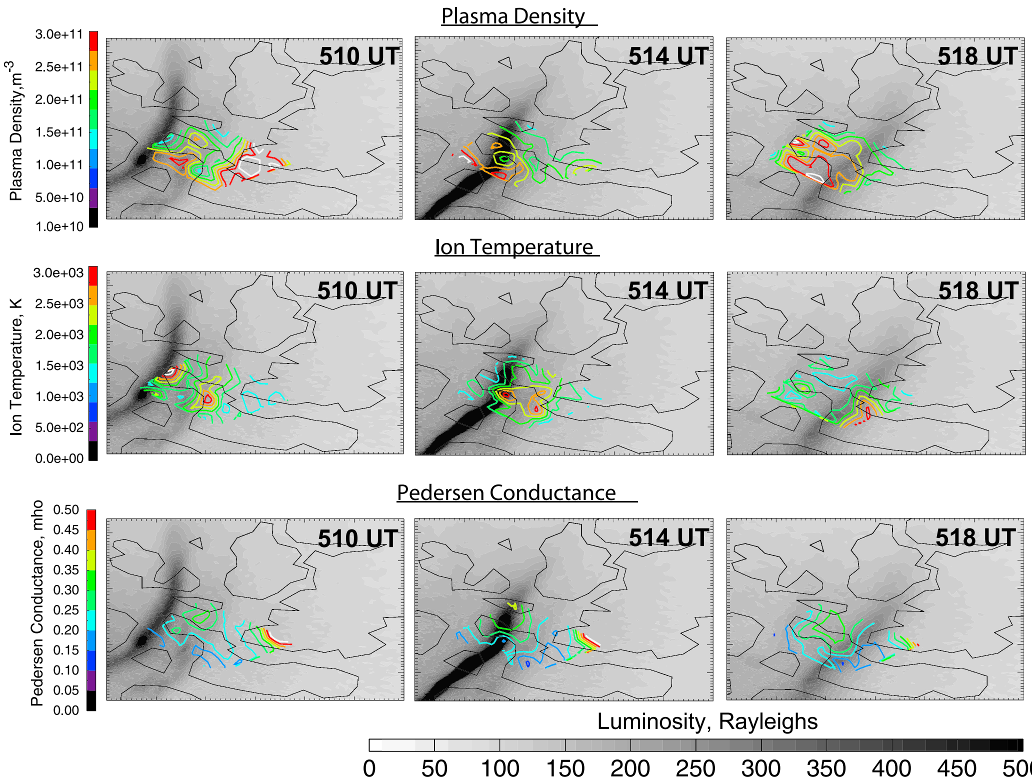

Figure 4. Combined plots of the optical data from OMTI (gray scale) and RISR-N contours for (top row) n_e, (middle row) $T_{i_{los}}$, and (bottom row) Σ_P. Dimensions of the FOV and the MLT meridians are indicated in Figure 1.

we are merely taking advantage of the large number of $\mathbf{v}_{los}$ measurements provided by the RISR-N system to constrain an estimate for ϕ, and subsequently $\mathbf{E}$. On its own, any monostatic radar system, including RISR-N, is unable to provide complete information about a plasma velocity vector for reasons described by *Freeman et al.* [1991].

To obtain estimates for the FAC, $\mathbf{J}_\parallel$, for the arc event, we enforce current closure, $\nabla \cdot \mathbf{J} = 0$, expressed as [*Sofko et al.*, 1995]

$$\mathbf{J}_\parallel = -\Sigma_P \cdot \mathbf{E}_\perp - \mathbf{E}_\perp \cdot \nabla\Sigma_P - \nabla\Sigma_H \cdot \mathbf{b} \times \mathbf{E}_\perp, \tag{4}$$

in which $\mathbf{b}$ is the geomagnetic field unit vector and $\mathbf{J}_\parallel \cdot \mathbf{b} > 0$; i.e., a positive FAC is parallel to the geomagnetic field. In this form, only measurements of the height-integrated Pedersen and Hall conductivities, Σ_P and Σ_H, and $\mathbf{E}_\perp$ are needed. The n_e measurements from RISR-N and neutral density estimates from Mass Spectrometer Incoherent Scatter (MSIS) [*Hedin*, 1991] are used to derive the conductivities which are then integrated along the geomagnetic field. Obtaining an estimate for $\mathbf{E}_\perp$ is done using the *Nicolls et al.* [2014] method previously described. The first two terms in equation (4) are the dominant terms given what we were able to ascertain about the conductivity gradients from the RISR-N data. For this experiment RISR-N was not able to provide reliable estimates of the Hall conductivities since they were so small. Therefore, the third term in equation (4) was dropped from our analysis. This has little effect on our $\mathbf{J}_\parallel$ estimates since Hall conductivities are generally much less than Pedersen conductivities above 200 km altitude [*Kelley*, 2009]—the altitudes which we will focus on. In this region we are also dealing with a lower limit of Σ_P, based on our knowledge of the *F* region contribution.

4. Results and Discussion

Contour plots of n_e, $T_{i_{los}}$, and estimates of Σ_P are plotted with the OMTI data in Figure 4. Estimates of $|\mathbf{E}_\perp|$ with vectors indicating the direction of the field and $\mathbf{J}_\parallel$ are plotted with the OMTI data in Figure 5. The altitude of the contours for n_e, $T_{i_{los}}$, Σ_P, and $\mathbf{J}_\parallel$ is centered at 325 km. The Σ_P estimates are a product of integrating the

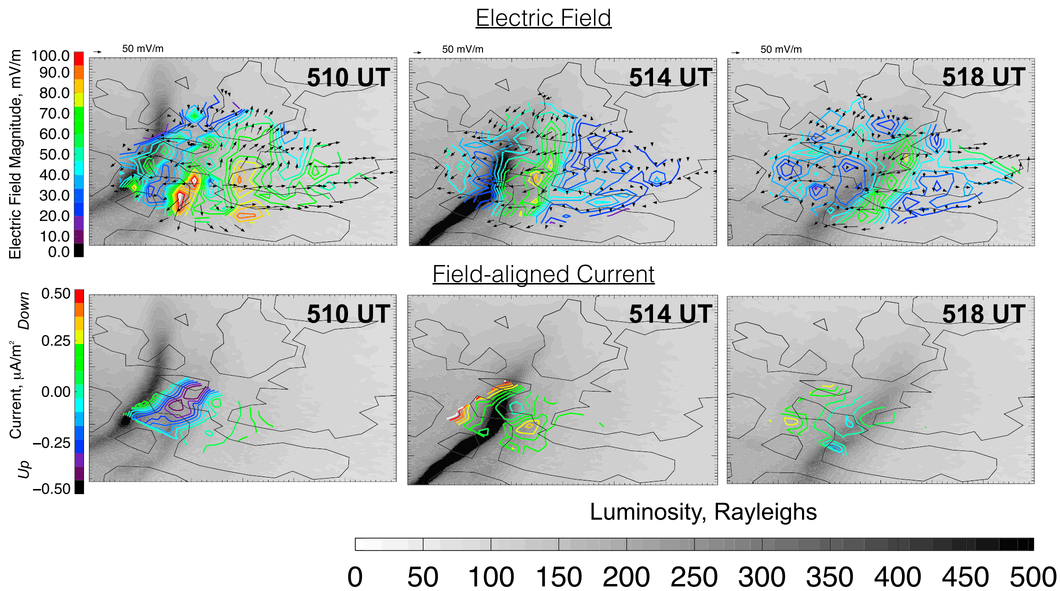

Figure 5. Combined plots of the optical data from OMTI (gray scale) and RISR-N contours for (top row) $|\mathbf{E}_\perp|$ with corresponding vectors, and (bottom row) $\mathbf{J}_\parallel$. Dimensions of the FOV and the MLT meridians are indicated in Figure 1.

Pedersen conductivities between 200 and 500 km altitude along the magnetic field. The $|\mathbf{E}_\perp|$ contours are constructed from data integrated over several hundred kilometers in altitude and mapped to 300 km altitude. The OMTI data are mapped to 250 km altitude, the normal practice for 630.0 nm emissions.

Structuring in $|\mathbf{E}_\perp|$ due to both arcs is significant and easily identifiable in Figure 5. Between 05:10 and 05:18 UT, meridionally extended $|\mathbf{E}_\perp|$ structures moved toward dawn, coincident with the two optical arcs discussed earlier. At 05:10 UT, three structures with low $|\mathbf{E}|$ were in the FOV. Two of the structures, both with $|\mathbf{E}| \sim 25$ mV/m, were collocated with two optical arcs shown in gray scale. The low $|\mathbf{E}_\perp|$ structures are indicative of the upward $\mathbf{J}_\parallel$ region of an arc; a region of electron precipitation in which plasma production is enhanced, increasing the ionospheric conductivities. The upward $\mathbf{J}_\parallel$ associated with the low $|\mathbf{E}_\perp|$ structure of the brightest of the arcs is estimated to be approximately 0.5 μA/m^2 at 05:10 UT, an intensity which declined during the transit of the arc through the RISR-N FOV. Enhancements in n_e due to the electron precipitation were also detected by RISR-N and are evident in Figure 2.

During the same time frame, a structure of substantially enhanced $|\mathbf{E}_\perp|$ was also present, moving toward dawn, ahead of the two low $|\mathbf{E}_\perp|$ features previously described. The structure measured nearly $|\mathbf{E}_\perp| \sim 125$ mV/m at 05:10 UT and remained above 75 mV/m for several minutes afterward. The $\mathbf{E}_\perp$ vectors coincident with the structure indicate that the electric field was predominantly directed toward dusk, toward the arc. This structure is the counterpart to the low electric field structure discussed earlier. It partially overlaps with a region of downward $\mathbf{J}_\parallel$. We postulate that the n_e depletion shown in Figures 2–4 is created in part by electrons moving upward, away from the region, thereby lowering the conductivity of the plasma and necessitating an increase in $|\mathbf{E}_\perp|$ to enforce current closure. This will be discussed in more detail shortly. A downward current, $\mathbf{J}_\parallel \sim 0.25$–$0.50$ μA/m^2, was in the vicinity of the enhanced $|\mathbf{E}_\perp|$ structure during the 05:10 to 05:18 UT time segment, as shown in Figure 5.

It should be noted that even though T_i is not a vector, when the electric field is strong (50 mV/m or greater) the observed value of T_i will depend on aspect angle, α, namely, the angle between the radar beam and the magnetic field direction. This is due to the significant anisotropic character of the ion velocity distribution in the F region under such circumstances [*St-Maurice and Schunk*, 1979]. It has been shown [*Raman et al.*, 1981] that the line-of-sight temperature is given by $T_{i_{\mathrm{los}}} = T_{i_\parallel} \cos^2\alpha + T_{i_\perp} \sin^2\alpha$. Analytical as well as Monte Carlo calculations of $T_{i_\parallel}$ and $T_{i_\perp}$ have been obtained for various situations of interest [e.g., *Winkler et al.*, 1992]. For example, $T_{i_{\mathrm{los}}}$ is of the order of 1000 K less than the actual temperature, T_i, at 125 mV/m for O^+ at 300 km altitude at an aspect angle of 30°. For the RISR-N beams used in the observations presented here the aspect angle varied between 20° for the high beam numbers and 50° for the low beam numbers. It is for this reason that we have chosen the $T_{i_{\mathrm{los}}}$ notation when referring to RISR-N measurements.

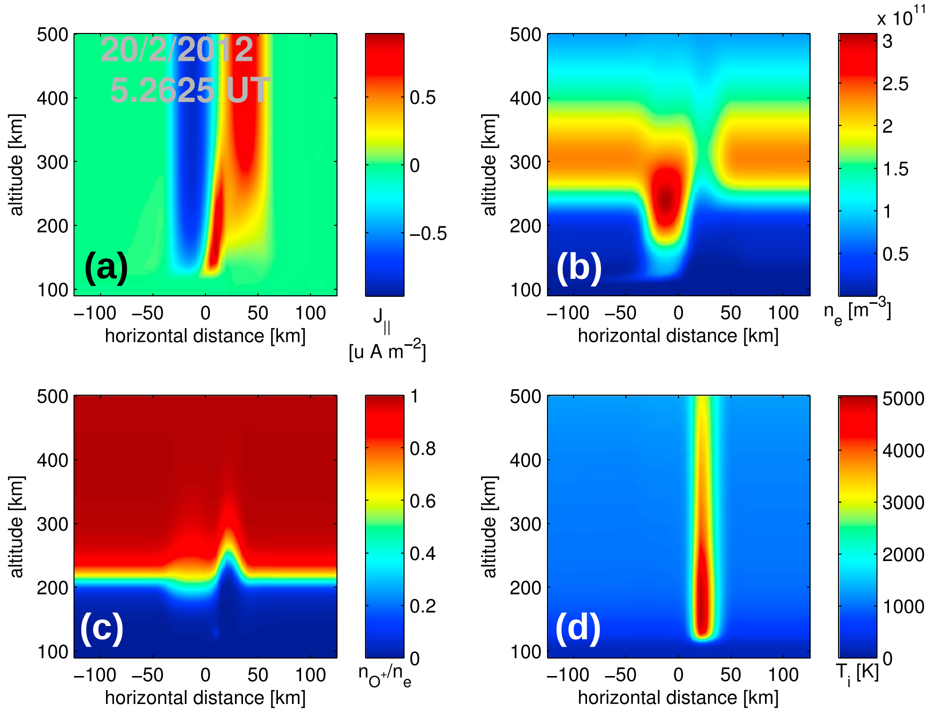

Figure 6. A 2-D snapshot of a simulation using the *Zettergren and Semeter* [2012] model, modified to replicate the observed density depletion at 05:16 UT, showing (a) $\mathbf{J}_{\|}$, (b) n_e, (c) the ratio n_{O+}/n_e, and (d) T_i. A movie of a simulation is given in Movie S2. The coincident location of the depletion leading the optical arc (where $\mathbf{J}_{\|} < 0$) and T_i enhancement is quite evident.

The downward $\mathbf{J}_{\|}$ region was responsible for considerable structuring of the polar cap ionosphere. This is evidenced by the grouping of the enhanced $|\mathbf{E}_{\perp}|$, enhanced $T_{i_{los}}$, and depleted n_e features near the downward $\mathbf{J}_{\|}$ region in Figure 5, eastward (dawnward) of the optical arc, and their simultaneous movements toward dawn. Velocity measurements from the Rankin Inlet Super Dual Auroral Radar Network (SuperDARN) radar [*Greenwald et al.*, 1995; *Chisham et al.*, 2007] also confirm velocity signatures consistent with a downward FAC on the leading edge of the arc, moving dawnward. However, the SuperDARN measurements were only line of sight and could not be fitted into full vectors [e.g., *Ruohoniemi and Baker*, 1998] due to the lack of coverage from other SuperDARN radars at the time. The measured increases in $T_{i_{los}}$ and a significant v_{los} reversal measured by RISR-N and SuperDARN (not shown), which can be seen in bottom panel of Figure 2 shortly after 05:00 UT, are symptomatic of frictional heating and augmented chemical recombination reaction rates—appealing candidates to account for the large n_e depletion [*Doe et al.*, 1995].

Evacuation of plasma via current closure must also be considered as a factor in the depletion [*Doe et al.*, 1993]. In this mechanism ions flow via Pedersen currents from a region of downward FAC toward the region of electron precipitation and accumulated negative charge, i.e., the optical arc. In the same downward FAC region, electrons flow vertically upward, thereby depleting the ionosphere coincident with the downward FAC region by the evacuation of plasma—both electrons and ions flow away from the downward FAC region.

Zettergren and Semeter [2012] reported an altitude dependence on chemical recombination and current closure mechanisms in the vicinity of a FAC system. The current closure mechanism [i.e., *Doe et al.*, 1993] dominates in the *E* region and lower *F* region, while the chemical recombination mechanism dominates in the *F* region, at least in the larger-scale currents (~10 km). Combining current closure (via Pedersen currents carried by the ions at the altitudes discussed here) with chemical recombination can culminate in a positive feedback if the FAC sourced by the magnetosphere is held constant: the decrease in n_e leads to an increase in $|\mathbf{E}_{\perp}|$ and n_e gradients; this increases the convection flows parallel to the arc, thereby heating up the ions, depleting n_e even more, forcing another increase in $|\mathbf{E}_{\perp}|$, etc.

For this study, the *Zettergren and Semeter* [2012] model was modified to reproduce the advecting FAC current system of the arc reported here. The plasma parameters measured by RISR-N were used as constraints to set a uniform background n_e. A background flux of 0.005 mW/m^2 of 100 eV electrons, uniform in time and space, representative of polar rain, was included. The boundary condition of the model consisted of an up/down FAC pair (i.e., the arc) of density 0.875 μA/m^2, a value consistent with the RISR-N estimates. A superposition of 0.15 mW/m^2, 500 eV electrons, and 0.2 mW/m^2, 50 eV electrons, was used for the arc precipitation in the model. The arc was then convected at 200 m/s to replicate the observed motion of the arc, and all other parameters such as T_i, T_e, n_e, $\mathbf{E}$, and $\mathbf{J}_{\parallel}$ on the interior part of the model domain were calculated as a function of time. A snapshot of a simulation at 05:16 UT is given in Figure 6, showing $\mathbf{J}_{\parallel}$, n_e, the ratio n_{O^+}/n_e, and T_i. A movie of the simulation results is given as supporting information Movie S2 (in which T_e and $v_{\parallel}$ for the event is also given). The n_{O^+}/n_e ratio is an output meant for the inspection of the conversion of O^+ to molecular ions, i.e., the production of O_2^+ and NO^+. The steep decline in the ratio at the location of the n_e depletion demonstrates that the depletion was generated in large part by chemical recombination. By inspection of Figure 6 and Movie S2, it is evident that the modified *Zettergren and Semeter* [2012] model reproduced the basic behavior of the n_e depletion near the upward $\mathbf{J}_{\parallel}$ region of the convecting arc. The arc produced a peak T_i enhancement roughly matching the data in Figure 4. The model was also able to reproduce the observed property of the depletion maintaining its position on the leading edge of the arc as it convected through the RISR-N field of view.

In Figure 5 there is evidence of structuring in $|\mathbf{E}_{\perp}|$ and $\mathbf{J}_{\parallel}$ that is not consistent with the singular arc system modeled here, namely, an arc system with a single upward and downward FAC channel. For example, at 05:14 and 05:18 UT, there is a downward FAC on the duskward (left of the optical arc) edge of the RISR-N FOV—the second downward FAC structure in that frame. This structure may either be evidence of a more complex FAC system associated with the arc, such as a second downward FAC region connected to the optical arc, or the second current structure may be associated with another arc which passed through the region minutes later. Our investigation focuses on a single arc system during a time period in which several arcs passed through the region. We may be underestimating the complexity of the system of currents and electric fields present in the region at the time.

Figure 4 shows that the depletion travels in conjunction with the leading edge of the arc for several minutes. Since there is no evidence of the depletion being generated within the RISR-N FOV we can conclude that it was generated several minutes before it entered the FOV. Results from *Zettergren and Semeter* [2012] support this, as well as their modified model outlined earlier. The convolution of heightened chemical recombination and current closure has the capacity to generate significant depletions of the *F* region plasma on the order of 15 min in simulation runs, drastically modifying the state parameters of the ionosphere. Chemical recombination dominates in generating the depletion in this event. Evacuation and recombination of the *E* and *F* regions have important implications for MI coupling in the polar ionosphere, for example, by structuring the Pedersen conductivity, which is an important component in the reflection coefficient of an Alfvén wave [*Zhu et al.*, 1993b].

The density features in Figure 2 are very coherent from beam to beam. At 250 m/s the depletion moved between RISR-N beams in roughly 2 min, which is likely why no substantial growth in the depletion can be seen when surveying all of the beams in the RISR-N FOV; the depletion moved through the FOV too quickly. Several trials of the *Zettergren and Semeter* [2012] model were conducted with the goal of reproducing a convecting arc and depletion pairing. Only those runs which featured a background plasma drift matching roughly that of the convecting arc replicated the observed pairing effect. When the background ionosphere was stationary with respect to the convecting arc, a depletion was still generated but it remained stationary and became partially filled in by the arc precipitation as the arc drifted past it.

According to Figure 6, the majority of the downward currents generated by the arc event is closing through the *F* region. Recall that RISR-N was unable to provide reliable conductivity estimates for altitudes below 200 km, so our analysis techniques could not be used to confirm the model results below that altitude. Nonetheless, the model results seem at least consistent with our understanding of the ionosphere at the time of this event. At nighttime, the *E* and *F* region conductivities are approximately equal [*Kelley*, 2009]. Prior to the event *E* region plasma density was extremely low, below the minimum threshold for reliable measurements with RISR-N. In the absence of any structured precipitation, which was the case before the arrival of the arc, any *E* region plasma density gradients would have been dissipated by chemistry. Thus, we should at least expect the dominant part of an FAC to close through the *F* region since its conductance is larger. The situation becomes much more complex when the arc is present; the arc may be able to produce sufficient ionization at lower altitudes, enabling more current to close there. We know this to be the case here since RISR-N detected a momentary n_e increase from 1 to 3×10^{10} m^{-3}, at 130 km altitude, and n_e enhancements higher up as well, as indicated in Figure 2. The modified *Zettergren and Semeter* [2012] model was investigated further by adjusting the energy spectrum of the background energy flux, representing the polar rain, for the simulations in this study. We found that the observed plasma density depletion was not generated for any of the cases in which the background energy flux was able to produce enough *E* region ionization to allow for more current to close there. Those energy fluxes resulted in high conductivities; the electric fields were too low to generate the observed plasma density depletion. We are therefore confident in what Figure 6 is showing: the majority of downward FACs during the arc event closed through the *F* region. Undoubtedly, our FAC analysis technique will always underestimate the arc FACs simply because the spatial resolution of RISR-N places a lower limit on our estimates of the n_e gradients. Furthermore, in the *E* region the ions quickly become collisional with decreasing altitude [*Sangalli et al.*, 2009], making it even more difficult to estimate the **E** from their measured drift. That said, Figure 6 supports our earlier implicit assumption that only applying equation (4) to altitudes above 200 km can still provide an accurate picture of the electrodynamics of the observed arc.

In the hours surrounding the arc event n_e exhibited appreciable variability; several polar cap patches were discernible in the OMTI and RISR-N data. A signature of one of the patches is seen in Figure 2 at 05:00 UT, immediately before the n_e depletion and arc were detected. It is conceivable that the quick decrease in n_e associated with the depletion feature was merely the signature of the tail-end of a patch advecting through the RISR-N beam; namely, $\partial n_e/\partial t = -\mathbf{v}_\mathrm{p} \cdot \nabla \mathrm{n}_\mathrm{e}$, in which $\mathbf{v}_p$ is the velocity of the patch. Even so, other features in Figures 2 and 3 show that an advecting patch could not be solely responsible for the n_e depletion feature. The depletion in Figures 2 and 3 marks the absolute minimum in n_e for the 2 h period; it is also an absolute minimum for a 6 h period surrounding the arc event. Furthermore, the depletion signature extends into the lower *F* region—into altitudes that are too low for patches. Therefore, other mechanisms such as chemical recombination must have been at play and were a leading contributor to generating the n_e depletion.

5. Conclusion

We have used multipoint measurements from RISR-N to, for the first time, resolve the electrodynamics and plasma structuring of a Sun-aligned arc in time and space. Estimates of a moderate $\mathbf{J}_\parallel$ associated with the arc were observed and are on par with previously reported arcs and models. $|\mathbf{E}_\perp|$ of the order of 100 mV/m and T_{i_los} of up to 3000 K were also measured in the vicinity of the arc. The arc was responsible for a significant enhancement of the ionospheric electric field and remarkable plasma structuring in the region. One of the most spectacular arc features was a prominent, meridionally extended n_e depletion, located partially within the auroral downward current region on the leading edge of the arc as it progressed toward dawn. The depletion was largely a by-product of heightened chemical recombination rates and was generated on a time scale of 15 min.

Our results are a consolidation of the electrodynamic, optical, and chemical properties of Sun-aligned arcs. They provide new insight into the nature of Sun-aligned arcs by demonstrating a clear and causal connection between the optical, plasma, and electrodynamic structuring of the arc. However, one major component which we were unable to provide here is the role of the *E* region and Hall conductivities. Ultimately, our calculations of $\mathbf{J}_\parallel$ underestimate the total currents produced by this event since we were unable to include the ionosphere below 200 km altitude in our analysis due to experimental uncertainty. This may be rectified by future multipoint measurements of the *E* region during a similar event, to investigate if the depletion mechanism is more current driven rather than chemically driven as it is in the *F* region.

Acknowledgments
The Resolute Bay Incoherent Scatter Radar (RISR-N) and the Resolute Bay Observatory (RBO) are operated by SRI International on behalf of the U.S. National Science Foundation under NSF Cooperative Agreement AGS-1133009. The RISR-N data featured in this article can be accessed at http://amisr.com/amisr/links/data-access/. The authors acknowledge the use of SuperDARN data. SuperDARN is a collection of radars funded by national scientific funding agencies of Australia, Canada, China, France, Japan, South Africa, United Kingdom, and United States of America. The SuperDARN data used in this work were collected with the support of the Canadian Space Agency's Geospace Observatory (GO Canada) continuation initiative. The SuperDARN data referenced in this article may be accessed by contacting J.-P. St.-Maurice (jp.stmaurice@usask.ca). OMTI data are available by contacting K. Shiokawa (shiokawa@stelab.nagoya-u.ac.jp). This work was supported in part by the Air Force Office of Scientific Research under contract FA9550-12-1-018 and by JSPS KAKENHI grants 16403007, 19403010, and 20244080. The authors thank the International Space Science Institute (ISSI, Bern, Switzerland) for sponsoring a series of international workshops during which some of this work was conducted. G.W.P. and J.P.S.M. were supported by NSERC and the Canada Research Chair program. M. Zettergren was supported by NSF grant AGS-1339537. G.W.P. dedicates this work to the memory of Bjorn Tokle, a son of Norway resting peacefully in Saskatchewan.

References

Bahcivan, H., R. Tsunoda, M. Nicolls, and C. Heinselman (2010), Initial ionospheric observations made by the new Resolute incoherent scatter radar and comparison to solar wind IMF, *Geophys. Res. Lett.*, *37*, L15103, doi:10.1029/2010GL043632.

Butler, T. W., J. Semeter, C. J. Heinselman, and M. J. Nicolls (2010), Imaging *F* region drifts using monostatic phased-array incoherent scatter radar, *Radio Sci.*, *45*, RS5013, doi:10.1029/2010RS004364.

Carlson, H. C., and S. W. H. Cowley (2005), Accelerated polar rain electrons as the source of Sun-aligned arcs in the polar cap during northward interplanetary magnetic field conditions, *J. Geophys. Res.*, *110*, A05302, doi:10.1029/2004JA010669.

Carlson, H. C., V. B. Wickwar, E. J. Weber, J. Buchau, J. G. Moore, and W. Whiting (1984), Plasma characteristics of polar cap *F*-layer arcs, *Geophys. Res. Lett.*, *11*, 895–898, doi:10.1029/GL011i009p00895.

Chisham, G., et al. (2007), A decade of the Super Dual Auroral Radar Network (SuperDARN): Scientific achievements, new techniques and future directions, *Surv. Geophys.*, *28*, 33–109, doi:10.1007/s10712-007-9017-8.

Cumnock, J. A., G. Le, S. Imber, J. A. Slavin, Y. Zhang, and L. J. Paxton (2011), Space technology 5 multipoint observations of transpolar arc related field-aligned currents, *J. Geophys. Res.*, *116*, A02218, doi:10.1029/2010JA015912.

Dahlgren, H., J. L. Semeter, K. Hosokawa, M. J. Nicolls, T. W. Butler, M. G. Johnsen, K. Shiokawa, and C. Heinselman (2012a), Direct three-dimensional imaging of polar ionospheric structures with the resolute bay incoherent scatter radar, *Geophys. Res. Lett.*, *39*, L05104, doi:10.1029/2012GL050895.

Dahlgren, H., G. W. Perry, J. L. Semeter, J.-P. St.-Maurice, K. Hosokawa, M. J. Nicolls, M. Greffen, K. Shiokawa, and C. Heinselman (2012b), Space-time variability of polar cap patches: Direct evidence, for internal plasma structuring, *J. Geophys. Res.*, *117*, A09312, doi:10.1029/2012JA017961.

Dahlgren, H., G. Perry, J.-P. St. Maurice, T. Sundberg, K. Hosokawa, J. L. Semeter, M. J. Nicolls, and K. Shiokawa (2014), 3D imaging reveals electrodynamics of polar cap aurora, *Astron. Geophys.*, *55*, 5.26–5.28, doi:10.1093/astrogeo/atu215.

de la Beaujardiere, O., R. Vondrak, and M. Baron (1977), Radar observations of electric fields and currents associated with auroral arcs, *J. Geophys. Res.*, *82*, 5051–5062, doi:10.1029/JA082i032p05051.

Doe, R. A., M. Mendillo, J. F. Vickrey, L. J. Zanetti, and R. W. Eastes (1993), Observations of nightside auroral cavities, *J. Geophys. Res.*, *98*, 293–310, doi:10.1029/92JA02004.

Doe, R. A., J. F. Vickrey, and M. Mendillo (1995), Electrodynamic model for the formation of auroral ionospheric cavities, *J. Geophys. Res.*, *100*, 9683–9696, doi:10.1029/95JA00001.

Fear, R. C., and S. E. Milan (2012), The IMF dependence of the local time of transpolar arcs: Implications for formation mechanism, *J. Geophys. Res.*, *117*, A03213, doi:10.1029/2011JA017209.

Fear, R. C., S. E. Milan, R. Maggiolo, A. N. Fazakerley, I. Dandouras, and S. B. Mende (2014), Direct observation of closed magnetic flux trapped in the high-latitude magnetosphere, *Science*, *346*, 1506–1510, doi:10.1126/science.1257377.

Freeman, M. P., J. M. Ruohoniemi, and R. A. Greenwald (1991), The determination of time-stationary two-dimensional convection patterns with single-station radars, *J. Geophys. Res.*, *96*, 15,735–15,749, doi:10.1029/91JA00445.

Greenwald, R. A., et al. (1995), DARN/SuperDARN, *Space Sci. Rev.*, *71*, 761–796, doi:10.1007/BF00751350.

Hedin, A. E. (1991), Extension of the MSIS thermosphere model into the middle and lower atmosphere, *J. Geophys. Res.*, *96*, 1159–1172, doi:10.1029/90JA02125.

Heinselman, C. J., and M. J. Nicolls (2008), A Bayesian approach to electric field and E-region neutral wind estimation with the Poker Flat Advanced Modular Incoherent Scatter Radar, *Radio Sci.*, *43*, RS5013, doi:10.1029/2007RS003805.

Hosokawa, K., J. I. Moen, K. Shiokawa, and Y. Otsuka (2011), Motion of polar cap arcs, *J. Geophys. Res.*, *116*, A01305, doi:10.1029/2010JA015906.

Kelley, M. C. (2009), *The Earth's Ionosphere: Plasma Physics and Electrodynamics, Int. Geophys. Ser.*, 2nd ed., Elsevier Sci., London, U. K.

Koustov, A. V., K. Hosokawa, N. Nishitani, K. Shiokawa, and H. Liu (2012), Signatures of moving polar cap arcs in the F-region PolarDARN echoes, *Ann. Geophys.*, *30*, 441–455, doi:10.5194/angeo-30-441-2012.

Kullen, A. (2012), Transpolar arcs: Summary and recent results, in *Auroral Phenomenology and Magnetospheric Processes: Earth And Other Planets, Geophys. Monogr. Ser.*, edited by A. Keiling et al., pp. 69–80, AGU, Washington, D. C., doi:10.1029/2011GM001183.

Nicolls, M. J., and C. J. Heinselman (2007), Three-dimensional measurements of traveling ionospheric disturbances with the Poker Flat Incoherent Scatter Radar, *Geophys. Res. Lett.*, *34*, L21104, doi:10.1029/2007GL031506.

Nicolls, M. J., R. Cosgrove, and H. Bahcivan (2014), Estimating the vector electric field using monostatic, multibeam incoherent scatter radar measurements, *Radio Sci.*, *49*, 1124–1139, doi:10.1002/2014RS005519.

Opgenoorth, H., I. Häggström, P. Williams, and G. Jones (1990), Regions of strongly enhanced perpendicular electric fields adjacent to auroral arcs, *J. Atmos. Terr. Phys.*, *52*, 449–458.

Raman, R. S. V., J. P. St-Maurice, and R. S. B. Ong (1981), Incoherent scattering of radar waves in the auroral ionosphere, *J. Geophys. Res.*, *86*, 4751–4762, doi:10.1029/JA086iA06p04751.

Ruohoniemi, J. M., and K. B. Baker (1998), Large-scale imaging of high-latitude convection with Super Dual Auroral Radar Network HF radar observations, *J. Geophys. Res.*, *103*, 20,797–20,811, doi:10.1029/98JA01288.

Sangalli, L., D. J. Knudsen, M. F. Larsen, T. Zhan, R. F. Pfaff, and D. Rowland (2009), Rocket-based measurements of ion velocity, neutral wind, and electric field in the collisional transition region of the auroral ionosphere, *J. Geophys. Res.*, *114*, A04306, doi:10.1029/2008JA013757.

Shiokawa, K., Y. Katoh, M. Satoh, M. K. Ejiri, T. Ogawa, T. Nakamura, T. Tsuda, and R. H. Wiens (1999), Development of Optical Mesosphere Thermosphere Imagers (OMTI), *Earth Planets Space*, *51*, 887–896, doi:10.5636/eps.51.887.

Sofko, G. J., R. Greenwald, and W. Bristow (1995), Direct determination of large-scale magnetospheric field-aligned currents with SuperDARN, *Geophys. Res. Lett.*, *22*, 2041–2044, doi:10.1029/95GL01317.

St-Maurice, J.-P., and R. W. Schunk (1979), Ion velocity distributions in the high-latitude ionosphere, *Rev. Geophys.*, *17*, 99–134, doi:10.1029/RG017i001p00099.

Winkler, E., J. P. St-Maurice, and A. R. Barakat (1992), Results from improved Monte Carlo calculations of auroral ion velocity distributions, *J. Geophys. Res.*, *97*, 8399–8423, doi:10.1029/91JA03104.

Zettergren, M., and J. Semeter (2012), Ionospheric plasma transport and loss in auroral downward current regions, *J. Geophys. Res.*, *117*, A06306, doi:10.1029/2012JA017637.

Zettergren, M., K. Lynch, D. Hampton, M. Nicolls, B. Wright, M. Conde, J. Moen, M. Lessard, R. Miceli, and S. Powell (2014), Auroral ionospheric F region density cavity formation and evolution: MICA campaign results, *J. Geophys. Res. Space Physics*, *119*, 3162–3178, doi:10.1002/2013JA019583.

Zhu, L., J. J. Sojka, R. W. Schunk, and D. J. Crain (1993a), A time-dependent model of polar cap arcs, *J. Geophys. Res.*, *98*, 6139–6150, doi:10.1029/92JA01600.

Zhu, L., J. J. Sojka, R. W. Schunk, and D. J. Crain (1993b), Influence of horizontal inhomogeneity in the ionosphere on the reflection of Alfven waves, *Geophys. Res. Lett.*, *20*, 313–316, doi:10.1029/93GL00079.

Zhu, L., R. Schunk, and J. Sojka (1997), Polar cap arcs: A review, *J. Atmos. Sol. Terr. Phys.*, *59*, 1087–1126, doi:10.1016/S1364-6826(96)00113-7.